

Structural, textural and photocatalytic properties of quantum-sized In_2S_3 -sensitized Ti-MCM-41 prepared by ion-exchange and sulfidation methods

Shaohua Shen, Liejin Guo*

State Key Laboratory of Multiphase Flow in Power Engineering, Xi'an Jiaotong University, Xi'an, Shaanxi 710049, PR China

Received 1 March 2006; received in revised form 13 April 2006; accepted 10 May 2006

Available online 19 May 2006

Abstract

In_2S_3 nanocrystallites were successfully encapsulated into the mesopores of Ti-MCM-41 by a two-step method involving ion-exchange and sulfidation. The X-ray diffraction (XRD) patterns, UV-vis absorption spectra (UV-Vis), high-resolution transmission electron microscopy (HRTEM) and N_2 adsorption–desorption isotherms were used to characterize the structure of the composite materials. It is found that the diameter of most In_2S_3 nanocrystallites is about 2.5 nm, less than the pore size of Ti-MCM-41. The In_2S_3 nanocrystallites inside the Ti-MCM-41 host show a significant blue-shift in the UV-vis absorption spectra. Under irradiation of visible light ($\lambda > 430$ nm), the composite material has much higher photocatalytic activity for hydrogen evolution than bulk In_2S_3 . It can be explained by the effective charge-separation in the quantum-sized In_2S_3 -sensitized Ti-MCM-41.

© 2006 Elsevier Inc. All rights reserved.

Keywords: Ti-MCM-41; Quantum-sized In_2S_3 ; Charge separation; Hydrogen evolution; Visible light

1. Introduction

Semiconductor metal oxides have received intense research interest for decades because of their activity for the photocatalytic water splitting [1]. Although there has been remarkable progress for photocatalysts working under ultraviolet light [2,3], the progress has rarely extended to the visible light region. Chalcogenides such as CdS have been studied extensively, since they have ideal edge positions of the valence and conduction bands for the reduction of water molecules [4]. Unfortunately, they have a fatal disadvantage of photocorrosion and hence are not useful for practical application. In recent researches [5–7], several new visible-light-driven photocatalyst materials for water splitting have been described. However, the highly efficient photocatalyst for water splitting under visible light irradiation has not been developed yet.

Because of the solid merits of controllable pore size, variable mesostructure, and functional composition, mesoporous

materials have attracted much attention in the fields of pure and applied sciences, since the invention of M41S mesoporous molecular sieves [8]. By utilizing the channel-typed nanospace of mesoporous materials, some unique chemical and physical properties have been introduced, such as selective chemical reactions [9], size-dependent molecular sieving [10], and controlled energy properties [11]. To provide additional functions to siliceous mesoporous materials, researchers have tried to being incorporated inorganic components such as transition metal ions and semiconductor nanocrystals within the framework and/or nanochannels of mesoporous silica materials. Several studies on nanocomposite systems containing inorganic guest species have revealed interesting functional properties in the areas of magnetism [12], optics [13], electronics [14], etc. Also, these derived composites play important role for advanced catalytic applications [15] and, in particular, for photocatalytic hydrogen evolution from water [16]. In the literature, it is thought that stability of the narrow-band-gap sulfide guest can be improved by being incorporated into the siliceous host [17], however, the photocatalytic activity of such composite is quite low, due to the dominant surface charge-recombination

*Corresponding author. Fax: +86 29 82669033.

E-mail address: lj-guo@mail.xjtu.edu.cn (L. Guo).

[18] in quantum-sized semiconductor guest confined in the mesopores of the host.

In other aspects, coupling two semiconductors may lead to an enhanced efficiency of photoinduced charge–carrier separation, as proved by the enhancement of photocatalytic [19] and photoelectrochemical [20] performances in combined materials. As is known, mesoporous silica materials consisting of Si and O atoms do not exhibit any absorption in the UV or visible light range. But then it is possible for silicate molecular sieves to exhibit optic property in the UV region by introducing Ti atoms into the molecular sieves framework. For example, Ti-MCM-41, a mesoporous molecular sieve having MCM-41 structure, shows a characteristic absorption band at 225 nm, which corresponds to the ligand-to-metal (–O–Ti–) electron transfer occurring at isolated Ti atoms [21]. In the case of photocatalysis, sensitizing the wide-band-gap semiconductor with another narrow-band-gap semiconductor has great influence on the charge–carrier recombination time and photoactive transition in the visible light which results in enhanced photocatalytic activity. Moreover, incorporating the narrow-band-gap semiconductor into the mesoporous Ti-MCM-41 host leads to different morphological and crystalline properties of the catalyst. Due to these remarkable reasons, sensitizing Ti-MCM-41 by incorporating some narrow-band-gap semiconductors into the mesopores of Ti-MCM-41 is viewed as one of the promising ways to explore novel catalyst. Two approaches have been generally used to transport precursor molecules or ions for assembly of nanoparticles or nanorods inside the channels of MCM-41 and related mesoporous materials. The first approach involves an ion-exchange procedure [22], the second one uses reversed micelles as an insertion carrier to incorporate nanoparticles into the mesoporous channels [23,24].

In this work, we focus on the preparation and investigation of quantum-sized In_2S_3 -sensitized Ti-MCM-41 composite semiconductor. For the synthesis, we used a two-step method involving ion-exchange and sulfidation to incorporate In_2S_3 into the mesopores of the Ti-MCM-41. This synthetic method generally allows controlling the texture and the morphological properties of the solid. The size of In_2S_3 nanoparticles is quantum-confined by the mesopores of the Ti-MCM-41 and less than the pore size of the Ti-MCM-41. Herein, we investigated the photocatalytic activity of quantum-sized In_2S_3 -sensitized Ti-MCM-41 composite semiconductor for hydrogen production from water under visible light irradiation ($\lambda > 430$ nm). The charge transfer mechanism in quantum-sized In_2S_3 -sensitized Ti-MCM-41 was also explored.

2. Experimental section

2.1. Synthesis

All chemical reagents used in the present experiments were obtained from commercial sources as guaranteed-

graded reagents and used without further purification. A typical synthesis process for preparation of mesoporous silica of Ti-MCM-41 follows the procedure [25] with minor modification: At 40 °C, 1.82 g of cetyltrimethylammonium bromide (CTAB) was dissolved into a solution containing 45 mL of deionized water and 0.42 g of NaOH, then 8.21 mL of tetrahydroxosilicate (TEOS) was added dropwise to the above solution and stirred vigorously for 1 h for the hydrolysis of TEOS. The resulted sol was stirred, and to which 0.25 g of tetrabutyl titanate (TBOT) was added dropwise and stirred at 40 °C for another 1 h. Finally the resulting gel was transferred to a 90-mL Teflon-lined autoclave and held at 100 °C for 3 days. The product obtained was filtered, washed with water and ethanol, and dried in air at 100 °C overnight. The as-synthesized samples were denoted as CTAB@Ti-MCM-41, and calcined at 500 °C in static air for 5 h to remove the template CTAB with a heating rate of 2 °C/min, then white powder Ti-MCM-41 was obtained. The molar ratio of Ti:Si is 0.02.

In_2S_3 nanoparticles were loaded inside the mesoporous Ti-MCM-41 through ion-exchange and sulfidation according to the literature [22]. The indium (III) methanol (MeOH) solution was prepared by dissolving 1.00 g of $\text{In}(\text{NO}_3)_3 \cdot 4.5\text{H}_2\text{O}$ in 100 mL of MeOH. The resulting solution was added to 1.00 g of the as-synthesized CTAB@Ti-MCM-41 powder. The slurry of the salt precursor and CTAB@Ti-MCM-41 was refluxed while being stirred for 4 h. The ion-exchanged Ti-MCM-41 was recovered by filtration and washed with excess MeOH and distilled water, to make sure that the In^{3+} absorbed onto the outer surface of Ti-MCM-41 was washed away. The product was then dried at 70 °C in vacuum for 6 h. Finally, treatment with H_2S at 300 °C for 3 h yielded the desired In_2S_3 nanoparticles inside Ti-MCM-41, denoted as In_2S_3 @Ti-MCM-41. The content of In_2S_3 in the final In_2S_3 @Ti-MCM-41 is 7.6 wt%.

Bulk In_2S_3 as reference was also prepared by treating 1.00 g of $\text{In}(\text{NO}_3)_3 \cdot 4.5\text{H}_2\text{O}$ with H_2S at 300 °C for 3 h in the muffle oven, product was denoted as bulk In_2S_3 .

2.2. Characterization

X-ray diffraction (XRD) patterns of the synthesized samples were obtained from a PANalytical X'pert MPD Pro diffractometer using Ni-filtered $\text{CuK}\alpha$ irradiation (wavelength 1.5406 Å). N_2 adsorption–desorption isotherms of samples were conducted at 77 K in the Beckman Coulter SA3100 plus instrument. Samples were degassed at 70 °C for 12 h prior to measurements. Pore size, surface area and pore volume of the samples were determined using the Barrett–Joyner–Halenda (BJH) [26], the Brunauer–Emmett–Teller (BET) and Horvath–Kawazoe (HK) [27] methods, respectively. Elemental Analysis was conducted on the Bruker S4 PIONEER X-ray fluorescence spectrum (XRF) using Ru target and 4 kW maximum power. Raman scattering study was performed on the

Jobin Yvon LabRAM HR Spectrometer with 514.5 nm irradiation from an argon ion laser at 20 mW. UV-vis absorption spectra (UV-vis) of the samples were measured on a HITACHI U4100 instrument equipped with labsphere diffuse reflectance accessory. High-resolution transmission electron microscopy (HRTEM) and the energy diffraction (ED) patterns were performed by a JEOL 3010 electron microscope.

2.3. Measurement of photocatalytic activity

Photocatalytic water splitting was performed in a Pyrex photoreactor. Hydrogen was analyzed in situ by gas chromatography (NaX zeolite column, TCD detector, nitrogen as carrier gas). 0.05 g of photocatalyst was dispersed in an aqueous Na_2SO_3 solution (0.38 mol L^{-1} , 50 mL), the mixture was irradiated with visible light ($\lambda \geq 430 \text{ nm}$) through a cut-off filter from a 350 W Xe lamp. A 2 wt%-Pt cocatalyst was photodeposited on the photocatalyst in situ using $\text{H}_2\text{PtCl}_6 \cdot \text{H}_2\text{O}$ [28]. Blank experiments revealed that no hydrogen was produced without catalyst added or light irradiation.

3. Results and discussion

Fig. 1 shows the Raman spectra of Ti-MCM-41 host. Four Raman bands at 482 , 805 , 970 and 1110 cm^{-1} are observed, the band at 482 cm^{-1} is ascribed to the symmetric stretching mode of the $[\text{SiO}_4]$ tetrahedron [29,30], and the other three Raman bands at 805 , 970 and 1110 cm^{-1} are assigned to the bending, symmetric stretching, and asymmetric stretching vibrations of Si–O–Ti [31,32], respectively. This is a strong evidence for some titanium atoms incorporated into the framework of Ti-MCM-41.

The UV-vis absorption spectra of Ti-MCM-41, In_2S_3 @Ti-MCM-41 and bulk In_2S_3 are shown in Fig. 2. The Ti-MCM-41 host does not exhibit any peaks by comparing to

the bulk TiO_2 , indicating that the titanium atoms are incorporated into the wall of the MCM-41 hexagonal structure and highly dispersed in silica matrixes as the isolated tetrahedrally coordinated Ti-oxides species [32,33], which corresponds to the result of the Raman spectra of Ti-MCM-41. Because no absorption for Ti-MCM-41 host is detected in the region of 400–800 nm, the absorption onset of In_2S_3 @Ti-MCM-41 at 550 nm shows the characteristic absorption of In_2S_3 nanoparticles, which is significantly blue-shifted relative to that of bulk In_2S_3 (650 nm). The significant blue shift in the absorption spectrum clearly indicates quantum confinement [34] of In_2S_3 nanoparticles inside the pores of Ti-MCM-41 host.

Mesostructural and ordered characteristics of the samples were manifested by XRD measurement. Fig. 3 shows the XRD patterns of Ti-MCM-41 host and In_2S_3 @Ti-MCM-41. Three reflection peaks are detected in Ti-MCM-41, which correspond to the characteristic of MCM-41 [8], indicating the presence of long-range hexagonal ordered structure in the Ti-MCM-41 host. But In_2S_3 @Ti-MCM-41 shows only one reflection peak (100), which indicates that the mesoporous structure of Ti-MCM-41 is less ordered after being loaded with In_2S_3 . Moreover, the (100) peak of In_2S_3 @Ti-MCM-41 demonstrates an obvious decrease in intensity, which should also be attributed to the filling of In_2S_3 nanoparticles. In the region of $2\theta = 20 - 80^\circ$, XRD patterns (Fig. 3, inset) of In_2S_3 @Ti-MCM-41 and bulk In_2S_3 both match well with that of cubic In_2S_3 (JCPDS card No. 03-065-0459). The estimated particle sizes of In_2S_3 in In_2S_3 @Ti-MCM-41 and bulk In_2S_3 calculated using the Scherrer equation [35] are about 2.54 and 43 nm, respectively. It is notable that the In_2S_3 nanoparticles were confined in the mesopores of the Ti-MCM-41 host. The diffraction peaks of In_2S_3 @Ti-MCM-41 are relatively broad due to nanoscale dimensions of the confined In_2S_3 .

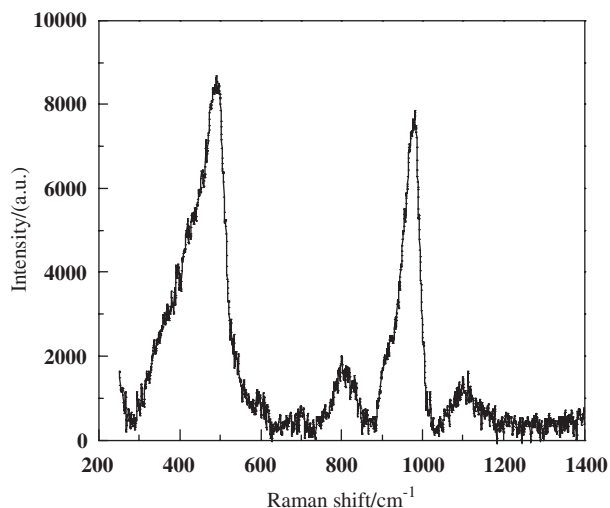


Fig. 1. Raman spectra of Ti-MCM-41.

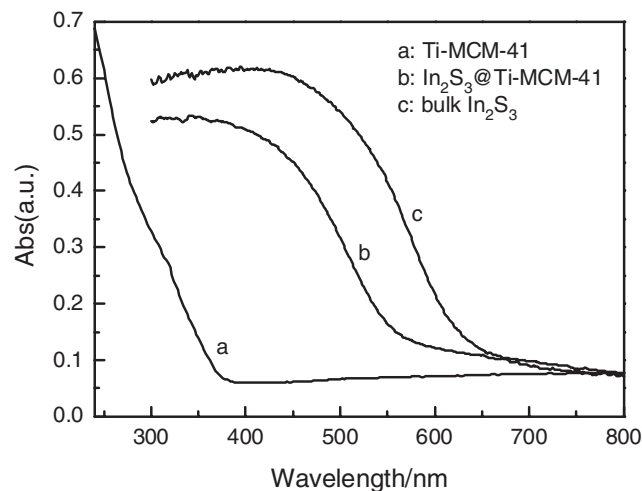


Fig. 2. UV-vis absorption spectra of Ti-MCM-41 (a), In_2S_3 @Ti-MCM-41 (b) and bulk In_2S_3 (c).

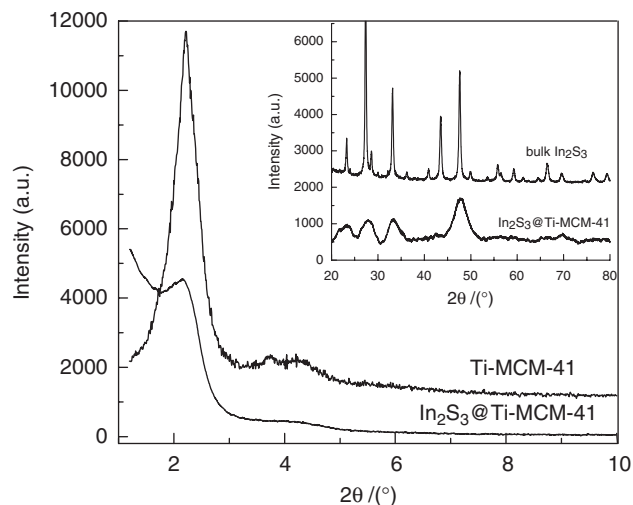


Fig. 3. XRD patterns of Ti-MCM-41 and In_2S_3 @Ti-MCM-41, inset is high-angle XRD patterns of bulk In_2S_3 and In_2S_3 @Ti-MCM-41.

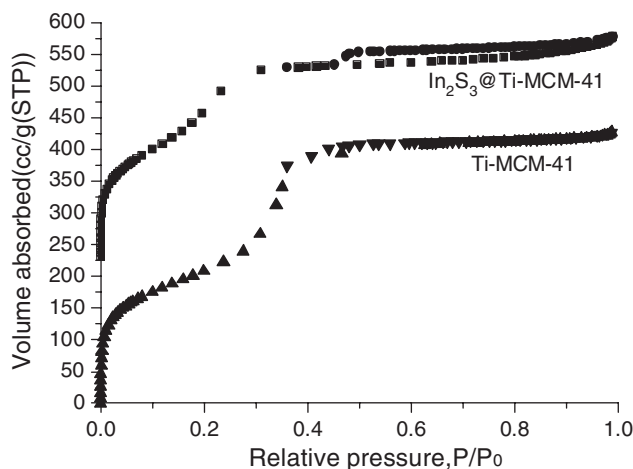


Fig. 4. N_2 adsorption–desorption isotherms of Ti-MCM-41 and In_2S_3 @Ti-MCM-41.

Fig. 4 shows the N_2 adsorption–desorption isotherms of Ti-MCM-41 and In_2S_3 @Ti-MCM-41 obtained at 77 K. Both of the isotherms are of type IV classification, which is typical adsorption of mesoporous materials [36]. The pore diameter of the Ti-MCM-41 host is about 3.15 nm, which is consistent with the estimated In_2S_3 particle size based on the width of the XRD peaks. Accordingly, In_2S_3 nanoparticles should be assembled inside the mesopores of Ti-MCM-41. The BET surface area, BJH pore diameter and pore volume of the samples are listed in Table 1. The decrease in BET surface area, BJH pore diameter and pore volume of In_2S_3 @Ti-MCM-41 in comparison with that of Ti-MCM-41 implies In_2S_3 clusters have been confined inside the mesopores of Ti-MCM-41 host.

A transmission electron microscopy (TEM) image of ordered Ti-MCM-41 host was recorded along the (001) direction (Fig. 5(a)). It is believed that the Ti-MCM-41 host possesses the long-range regular hexagonal arrange-

Table 1

Pore structure parameters of Ti-MCM-41 and In_2S_3 @Ti-MCM-41

Sample	Surface area (m ² /g)	Pore size (nm)	Pore volume (cm ³ /g)
Ti-MCM-41	892	3.15	0.256
In_2S_3 @Ti-MCM-41	753	2.73	0.196

ment of the pores, the size of the pores can be as large as 3.0 nm, corresponding to the results of the BJH pore diameter obtained from the N_2 adsorption–desorption isotherms. The In_2S_3 @Ti-MCM-41 was further investigated by HRTEM to gain insight into the filling of the pores and to get additional information about the possible presence of non-nanoscale material outside the pores and on the surface of the Ti-MCM-41 host. As can be seen from Fig. 5(b), the In_2S_3 nanoparticles are confined in the pores of the Ti-MCM-41 host as the arrow shown, no additional material outside the pores was found and no separate phase of macroscale In_2S_3 was outside the host. The diameter of these nanoparticles is about 2.5 nm due to the limitation of Ti-MCM-41 mesopores, which is consistent with estimated In_2S_3 particle size based on the width of the XRD peaks. However, the mesoporous structure of In_2S_3 @Ti-MCM-41 is less ordered, maybe due to the formation of In_2S_3 in the mesopores of Ti-MCM-41 and calcination at 300 °C in the H_2S atmosphere, which will destroy the mesostructure of Ti-MCM-41 to some extent.

The EDS analysis on the selected region in Fig. 5(b) reveals In and S signals, as shown in Fig. 5(c). The elements of Si, O, Ti and Cu (from support grid) are also detected. From the EDS spectrum, the atomic ration of In to S is 2.07:3.33, which is close to 2:3 and further confirms the formation of In_2S_3 nanoparticles inside the Ti-MCM-41 host.

XRF analysis result confirms that the content of In_2S_3 in the In_2S_3 @Ti-MCM-41 sample is 7.6 wt%. Fig. 6 shows H_2 evolution under visible light ($\lambda > 430$ nm) irradiation from an aqueous solution containing the sacrificial reagents SO_3^{2-} (pH 8.8) [37] over In_2S_3 @Ti-MCM-41 and bulk In_2S_3 with and without of Pt cocatalyst. During the photocatalytic reaction, the activity of In_2S_3 @Ti-MCM-41 remained quite stable over 30 h when the reaction system was flushed periodically with nitrogen, the rate of hydrogen evolution reached about $12.5 \mu\text{mol h}^{-1} \text{g}_{\text{In}_2\text{S}_3}^{-1}$. Moreover, the activity of In_2S_3 @Ti-MCM-41 was much improved by loading Pt cocatalyst, reaching about $38 \mu\text{mol h}^{-1} \text{g}_{\text{In}_2\text{S}_3}^{-1}$. However, as shown in the figure, the photoactivity of bulk In_2S_3 was rather low even with Pt cocatalyst.

The photocatalytic activity is governed by the separation of photogenerated electron–hole, and efficiency of the reaction of electrons and holes with their respective reactants. In the In_2S_3 @Ti-MCM-41 composite, only quantum-sized In_2S_3 can be excited by visible light, and for In_2S_3 , the electron–hole recombination may be grouped

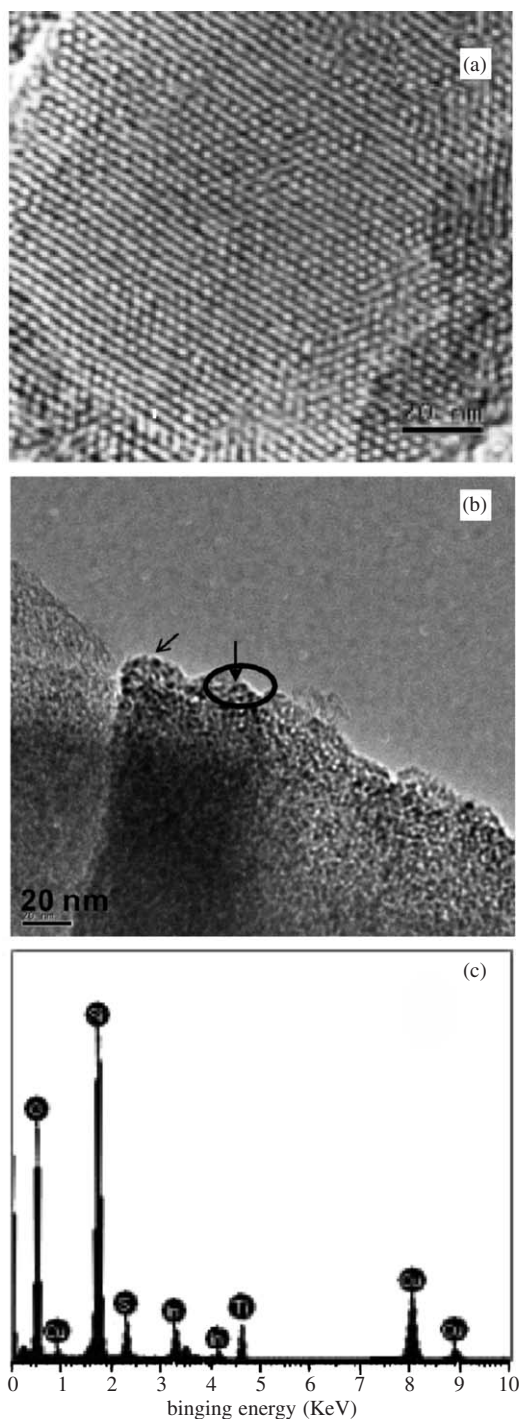


Fig. 5. HRTEM images of Ti-MCM-41 (a), In_2S_3 @Ti-MCM-41 (b), and EDS spectrum of In_2S_3 @Ti-MCM-41 (c).

into two categories: volume recombination and surface recombination. On the one hand, volume recombination, which is a dominant process in the large In_2S_3 particles, can be reduced by decreasing particle size [18] via incorporating the particles into the mesopores of Ti-MCM-41. Most of the electron–hole pairs generated in the quantum-sized In_2S_3 are sufficiently close to the surface. They may quickly reach the surface rather than recombine in volume of the

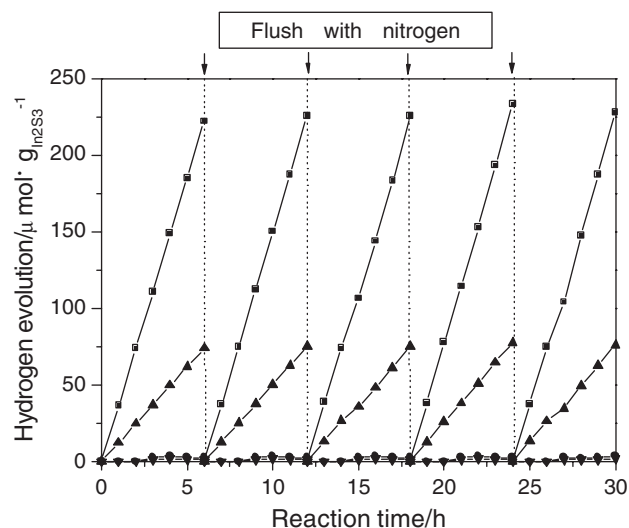


Fig. 6. Hydrogen evolution over $\text{Pt-In}_2\text{S}_3$ @Ti-MCM-41 (■), In_2S_3 @Ti-MCM-41 (▲), Pt-bulk In_2S_3 (◆), bulk In_2S_3 (▼) under visible light irradiation ($\lambda > 430$ nm).

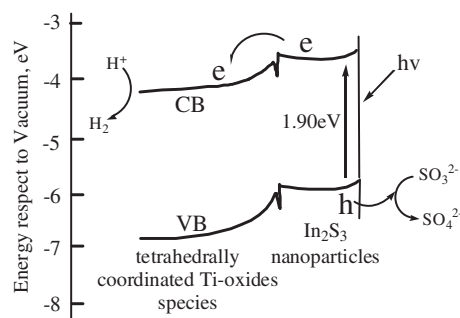


Fig. 7. Proposed band energy diagram for In_2S_3 @Ti-MCM-41 in an aqueous Na_2SO_3 solution (pH = 8.8).

In_2S_3 particle, and will undergo rapid surface recombination at the surface trapping sites owing to the lack of driving force for electron–hole pairs separation. On the other hand, coupling two semiconductors has a beneficial role in improving charge separation, as mentioned earlier [19,38]. This idea can be rationalized in the In_2S_3 @Ti-MCM-41 composite, in which the surface recombination of electron–hole pairs on the quantum-sized In_2S_3 is greatly suppressed at the In_2S_3 /Ti-oxides species interface. Fig. 7 shows the proposed band energy diagram for the In_2S_3 @Ti-MCM-41 deduced from those for In_2S_3 and TiO_2 [39]. The flat band potential of tetrahedrally coordinated Ti-oxides species imbedded in the Ti-MCM-41 host lies more positive than that of the quantum-sized In_2S_3 in the In_2S_3 @Ti-MCM-41 composite, thus charge separation takes place at the In_2S_3 /Ti-oxides species interface. Photo-induced electrons in the conduction band of In_2S_3 move to the In_2S_3 /Ti-oxides species interface with a high tendency due to energy gradient in the space charge layer. These electrons are transferred to the conduction

band of the Ti-oxides species by jumping over the small discontinuity of both conduction bands at the interface. Such an electron transfer could prevent the charge-recombination on the surface of quantum-sized In_2S_3 , and the energy difference at the In_2S_3 /Ti-oxides species interface prevents the reverse flow of the electrons. As is explained above, in the In_2S_3 @Ti-MCM-41 composite, the effective electron–hole separation in volume and on surface can be attributed to the quantum size of the In_2S_3 and coupling of In_2S_3 with the Ti-MCM-41 host, respectively. This may be the rational reason why the photocatalytic activity of the In_2S_3 @Ti-MCM-41 composite is higher than that of bulk In_2S_3 .

Another possible reason for high photocatalytic activity of In_2S_3 @Ti-MCM-41 can be attributed to the effective reaction of electron and hole with reactants [40]. The surface area up to $753 \text{ m}^2/\text{g}$, much higher than that of bulk In_2S_3 ($7.18 \text{ m}^2/\text{g}$), makes the photoexcited electrons in In_2S_3 @Ti-MCM-41 composite more accessible to water molecules to reduce H^+ [41]. Meanwhile, the high surface area can also avail the holes to contact and react with the sacrificial reagents (SO_3^{2-}) in time, rather than react with the In_2S_3 itself, hence preventing the photocorrosion of In_2S_3 in the In_2S_3 @Ti-MCM-41 composite.

4. Conclusions

In summary, the combined results of XRD, HRTEM, N_2 adsorption–desorption isotherms and UV-vis absorption spectrum proved that the In_2S_3 nanoparticles have been successfully encapsulated into and confined inside the mesopore of Ti-MCM-41 by a simple two-step procedure involving ion-exchange and sulfidation. Compared to bulk In_2S_3 , the In_2S_3 @Ti-MCM-41 composite shows a significant blue shift in the UV-vis absorbance spectra, and the size of In_2S_3 particles is about 2.5 nm, in accordance with the pore size of the Ti-MCM-41 host (about 3.1 nm). The developed In_2S_3 @Ti-MCM-41 composite exhibited much better photocatalytic activity than bulk In_2S_3 in hydrogen production reaction from water under visible light irradiation. The confined size of incorporated In_2S_3 and coupling In_2S_3 with Ti-MCM-41, respectively, suppress the volume recombination and surface recombination of the electron–hole pairs in the quantum-sized In_2S_3 -sensitized Ti-MCM-41 composite. The concept of such size control of confined nanomaterials in the Ti-MCM-41 host will hopefully provide a facile route for developing advanced composite semiconductors applied in photocatalysis.

Acknowledgments

The authors gratefully acknowledge the financial supports of the National Natural Science Foundation of China (No. 50521604) and National Basic Research Program of China (No. 2003CB214500).

References

- [1] K. Honda, A. Fujishima, *Nature* 238 (1972) 37–38.
- [2] H.G. Kim, D.W. Hwang, J. Kim, Y.G. Kim, J.S. Lee, *Chem. Commun.* 12 (1999) 1077–1078.
- [3] J. Sato, N. Saito, H. Nishiyama, Y. Inoue, *J. Phys. Chem. B* 107 (2003) 7965–7969.
- [4] M. Koca, M. Sahin, *Int. J. Hydrogen Energy* 27 (2002) 363–367.
- [5] Z. Zou, J. Ye, K. Sayama, H. Arakawa, *Nature* 414 (2001) 625–627.
- [6] D.W. Hwang, H.G. Kim, J.S. Lee, J. Kim, W. Li, S.H. Oh, *J. Phys. Chem. B* 109 (2005) 2093–2102.
- [7] Z. Lei, G. Ma, M. Liu, W. You, H. Yan, G. Wu, T. Takata, M. Hara, K. Domen, C. Li, *J. Catal.* 237 (2006) 322–329.
- [8] J.S. Beck, J.C. Vartuli, W.J. Roth, M.E. Leonowicz, C.T. Kresge, K.D. Schmitt, C.T.W. Chu, D.H. Olson, E.W. Sheppard, S.B. McCullen, J.B. Higgins, J.L. Schlenker, *J. Am. Chem. Soc.* 114 (1992) 10834–10843.
- [9] J.Y. Ying, C.P. Mehnert, M.S. Wong, *Angew. Chem. Int. Ed.* 38 (1999) 56–77.
- [10] J.M. Kisler, A. Dahler, G.W. Stevens, A.J. O'Connor, *J. Micropor. Mesopor. Mater.* 44–45 (2001) 769–774.
- [11] V.I. Srdanov, I. Alxneit, G.D. Stucky, C.M. Reaves, S.P. DenBaars, *J. Phys. Chem. B* 102 (1998) 3341–3344.
- [12] A.F. Gross, M.R. Diehl, K.C. Beverly, E.K. Richman, S.H. Tolbert, *J. Phys. Chem. B* 107 (2003) 5475–5482.
- [13] M.D. Perez, E. Otal, S.A. Bilmes, G.J.A.A. Soler-Illia, E.L. Crepaldi, D. Grosso, C. Sanchez, *Langmuir* 20 (2004) 6879–6886.
- [14] B.J. Scott, G. Wirsberger, G.D. Stucky, *Chem. Mater.* 13 (2001) 3140–3150.
- [15] C.-H. Lee, T.-S. Lin, C.-Y. Mou, *J. Phys. Chem. B* 107 (2003) 2543–2551.
- [16] T. Hirai, H. Okubo, I. Komasa, *J. Phys. Chem. B* 103 (1999) 4228–4230.
- [17] Z. Lei, W. You, M. Liu, G. Zhou, T. Takata, M. Hara, K. Domen, C. Li, *Chem. Commun.* 17 (2003) 2142–2143.
- [18] Z.B. Zhang, C.C. Wang, R. Zakaria, J.Y. Ying, *J. Phys. Chem. B* 102 (1998) 10871–10878.
- [19] G. Guan, T. Kida, K. Kusakabe, K. Kimura, E. Abe, A. Yoshida, *Appl. Catal. A: Gen.* 295 (2005) 71–78.
- [20] P.M. Sirimanne, Y. Yasaki, N. Sonoyama, T. Sakata, *Mater. Chem. Phys.* 78 (2003) 234–238.
- [21] S.H. Liu, P.H. Wang, Y.J. Huang, Y.M. Sun, K.S. Lin, M.C. Hsiao, *Energy Sources* 25 (2003) 591–595.
- [22] Z. Zhang, S. Dai, X. Fan, D.A. Blom, S.J. Pennycook, Y. Wei, *J. Phys. Chem. B* 105 (2001) 6755–6758.
- [23] W.-S. Chae, J.-H. Ko, I.-W. Hwang, Y.-R. Kim, *Chem. Phys. Lett.* 365 (2002) 49–56.
- [24] T. Hirai, H. Okubo, I. Komasa, *J. Colloid Interface Sci.* 235 (2001) 358–364.
- [25] W. Zhang, M. Froba, J. Wang, P.T. Tanev, J. Wong, T.J. Pinnavaia, *J. Am. Chem. Soc.* 118 (1996) 9164–9171.
- [26] E.P. Barrett, L.G. Joyner, P.P. Halenda, *J. Am. Chem. Soc.* 73 (1951) 373–380.
- [27] R.E. Reddy, L. Davydov, P.G. Smirniotis, *J. Phys. Chem. B* 106 (2002) 3394–3401.
- [28] D. Wang, Z. Zou, J. Ye, *Chem. Phys. Lett.* 411 (2005) 285–290.
- [29] P.K. Dutta, J.A. Incavo, *J. Phys. Chem.* 91 (1987) 4443–4446.
- [30] P.K. Dutta, K.M. Rao, J.Y. Park, *J. Phys. Chem.* 95 (1991) 6654–6656.
- [31] C. Li, G. Xiong, Q. Xin, J. Liu, P. Ying, Z. Feng, J. Li, W. Yang, *Angew. Chem. Int. Ed.* 38 (1999) 2220–2222.
- [32] J. Yu, Z. Feng, L. Xu, M. Li, Q. Xin, Z. Liu, C. Li, *Chem. Mater.* 13 (2001) 994–998.
- [33] Y. Hu, S. Higashimoto, G. Martra, J. Zhang, M. Matsuoka, S. Coluccia, M. Anpo, *Catal. Lett.* 90 (2003) 161–163.
- [34] G.D. Stucky, J.E. Mac Dougail, *Science* 247 (1990) 669–678.
- [35] W. Xu, Y. Liao, D.L. Akins, *J. Phys. Chem. B* 106 (2002) 11127–11131.

- [36] K.S.W. Sing, D.H. Everett, R.A.W. Haul, L. Moscou, *Pure Appl. Chem.* 57 (1985) 603–619.
- [37] L.Y. Chen, S. Jaenicke, G.K. Chuah, *Micropor. Mater.* 12 (1997) 323–330.
- [38] K.R. Gopidas, M. Bohorquez, P.V. Kamat, *J. Phys. Chem.* 94 (1990) 6435–6440.
- [39] Y. Xu, M.A.A. Schoonen, *Am. Mineral.* 85 (2000) 543–556.
- [40] X. Wang, J.C. Yu, C. Ho, Y. Hou, X. Fu, *Langmuir* 21 (2005) 2552–2559.
- [41] M.P. Kapoor, S. Inagaki, H. Yoshida, *J. Phys. Chem. B* 109 (2005) 9231–9238.